ACS APPLIED NANO MATERIALS

www.acsanm.org Article

PtRu Catalysts on Nitrogen-Doped Carbon Nanotubes with Conformal Hydrogenated TiO_2 Shells for Methanol Oxidation

Archana Sekar, Nathaniel Metzger, Sabari Rajendran, Ayyappan Elangovan, Yonghai Cao, Feng Peng, Xianglin Li, and Jun Li*

Cite This: *ACS Appl. Nano Mater.* 2022, 5, 3275−3288 Read Online

ACCESS | Metrics & More | Article Recommendations | Supporting Information

ABSTRACT: The methanol oxidation reaction (MOR) is the limiting factor in direct methanol fuel cells (DMFC). There is an urgent need to improve the catalytic activity and stability of MOR catalysts. This study reports a highly active PtRu catalyst for MOR based on a hybrid multifunctional catalyst support consisting of a conformal amorphous hydrogenated TiO_2 shell wrapped around the oxygenated N-doped carbon nanotube core, denoted as PtRu/TiO_2/ONCNT-400. Both the TiO_2 shell and the subsequent PtRu nanoparticles are deposited by a rapid microwave-assisted synthesis processes. The hydrogenated TiO_2 shell is found to exhibit a strong interaction with the deposited PtRu catalyst nanoparticles and effectively prevent them from agglomeration during the post-deposition thermal annealing to form more active crystalline PtRu alloy catalysts. In addition, the defective hydrogenated TiO_2 shell enhances the PtRu catalyst activity by the synergistic effects of partial charge transfer from TiO_2 to PtRu and high oxophilicity, which improves the kinetics of oxidation of poisonous CO intermediate to CO_2. The mass activity for MOR and long-cycling stability of the PtRu/TiO_2/ONCNT-400 catalyst surpass the two benchmark commercial PtRu/C catalysts from Johnson Matthey (JM) and Tanaka KiKinzoku (TKK), respectively. The results demonstrate that PtRu/TiO_2/ONCNT-400 can serve as an efficient catalyst for MOR in DMFC.

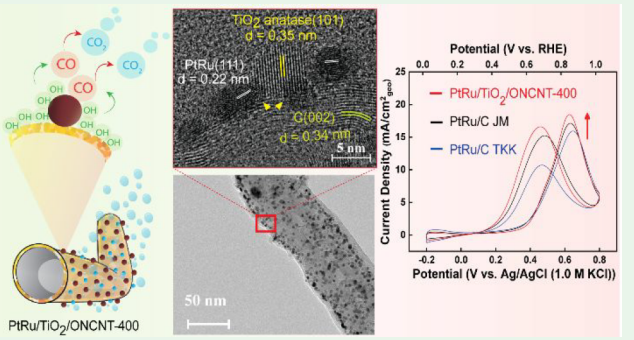

KEYWORDS: *hydrogenated TiO_2, ultrathin shell, microwave synthesis, PtRu nanoparticles, methanol oxidation reaction (MOR), CO oxidation, strong metal−support interaction (SMSI)*

1. INTRODUCTION

The ever-increasing demand for replacing fossil fuels has stimulated the investigation of renewable energy conversion devices such as fuel cells.[1−3] Direct Methanol Fuel Cells (DMFCs), a type of proton exchange membrane fuel cell (PEMFC), have attracted considerable attention owing to the low cost, high energy density (6.08 kWh/kg for liquid methanol), and ease in handling methanol fuels.[1] However, sluggish kinetics of the methanol oxidation reaction (MOR) and severe methanol crossover limit the power density and conversion efficiency that can be obtained, which hinders the commercialization of DMFCs. At present, platinum (Pt) is the primary choice of electrocatalyst for catalyzing MOR.[4,5] However, the strong adsorption of methanol oxidation intermediates such as carbon monoxide (CO) on Pt surface causes poisoning of the Pt catalysts and impedes the MOR.[3,6] General strategies to overcome this issue is to incorporate other precious platinum group metals (PGMs) or transition metals (TMs) to form binary alloys, such as PtRu, PtPd, PtCu, PtRh, PtCo, and PtMo,[7] which can provide abundant hydroxyl species and exhibit electronic ligand effects on Pt to efficiently oxidize CO to CO_2, thus improving the MOR kinetics. To date, PtRu nanoparticles (NPs) on nanoscale carbon supports, i.e., PtRu/C, is the state-of-the-art MOR catalyst in acidic medium owing to its excellent mass activity.[8] Nevertheless, the dissolution of PtRu NPs due to carbon corrosion during fuel cell operations, particularly at the start-up/shut-down processes[9] still limits the durability of PtRu/C catalysts in DMFCs. There is a strong demand for the design and development of highly active electrocatalyst and catalyst supports which can impart a strong metal−support interaction (SMSI)[10,11] to improve the catalyst stability.

Various graphitic nanocarbon supports such as carbon nanotubes (CNTs),[12] carbon nanofibers (CNFs), and graphene were studied to reduce carbon corrosion in PEMFCs owing to their intrinsic high chemical stability and outstanding electronic conductivity.[11,13−15] Among these, several reports

Received: November 5, 2021
Accepted: December 28, 2021
Published: January 6, 2022

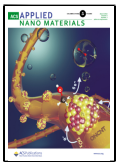

https://doi.org/10.1021/acsanm.1c03742
ACS Appl. Nano Mater. 2022, 5, 3275−3288

demonstrate that nitrogen (N) doping in graphitic carbon supports not only enhances the stability but also increases the activity of PGM NPs toward MOR due to the SMSI provided at the doped graphitic edges of the support.[16−18] Recently, our group reported the enhanced MOR activity and stability of Pt and PtRu NPs deposited on N-doped vertically aligned carbon nanofibers (N-VACNFs) owing to the SMSI provided by the graphitic edge and N-doping.[19] We revealed that the electron transfer between PGM catalysts and the N-VACNF support promotes the binding of OH^- over CO on the Pt surface, which accelerated the oxidation of CO to CO_2. In addition, the oxygenated functional groups present on the N-VACNFs made the carbon surface more oxophilic, which assisted efficient CO oxidation at the neighboring Pt sites.[19,20] Hence, graphitic carbon supports with synergistic enhancement by N-doping and oxygenation are potential candidates for MOR co-catalysts and catalyst supports.

In other circumstances, metal oxides such as IrO_2, CeO_2, RuO_2, and TiO_2 were studied as co-catalysts, non-carbon catalyst supports, and hybrid catalyst supports to enhance the catalytic activity and stability of Pt-based electrocatalysts since the metal oxides can effectively hinder carbon corrosion in PEMFCs, including DMFCs.[10,21] Among them, TiO_2 is the most promising candidate due to its low cost, superior corrosion resistance in fuel cell operation conditions, and strong interaction with PGM NPs. TiO_2 serves multiple functions, including preventing the PGM NP agglomeration during high-temperature annealing and providing abundant hydroxyl species to accelerate CO oxidation to CO_2.[22−25] For example, Huang et al. showed enhanced power density and stability of Pt electrocatalysts using corrosion-resistant TiO_2 as the support based on SMSI.[26] However, the wide bandgap (3.2 eV) makes the pristine TiO_2 an intrinsically poor electronic conductor (with a conductivity in the order of 10^{-7} S/cm).[27] To increase the electronic conductivity, Ioroi et al. reported the synthesis of substoichiometric Magneli phase TiO_2 (Ti_nO_{2n-1}) by reducing TiO_2 in a hydrogen atmosphere at ∼1050 °C and using it as a Pt catalyst support for PEMFCs.[28] The Ti_4O_7 phase exhibits an increased electronic conductivity to the order of 10^3 S/cm.[28,29] Several other researchers reported that doping metal or nonmetal atoms into TiO_2 lattice can increase the electronic conductivity.[30−33] However, the above-mentioned strategies involve thermal treatment of metal oxides at high temperatures (>1000 °C), which cause particle agglomeration and decrease the specific surface area (SSA). This limits its ability to support well-dispersed electrocatalysts. Recent studies show that defect engineering in TiO_2 lattice, without phase change, by inducing oxygen vacancies with thermal annealing TiO_2 at relatively lower temperature (∼300 to 500 °C) in hydrogen atmosphere, has the potential in improving the electronic conductivity of TiO_2, as the delocalized electrons near the oxygen vacancies can be excited easily to the conduction band.[34,35] For example, the black TiO_2 anatase nanocrystals (otherwise called hydrogenated TiO_2) synthesized by Chen et al. have attracted a lot of attention due to enhanced solar light absorption for photocatalysis provided by the oxygen vacancies and Ti^{3+} lattices in the disordered black TiO_2 layers.[34,36,37] Followed by that, Myung et al. reported the synthesis of black TiO_2 anatase nanocrystals (bandgap of about ∼1.8 eV) for ultrafast Li^+ insertion into and extraction from the anatase TiO_2 host, making it a unique high-rate electrode for Li-ion batteries.[27] Zhang et al. showed improved activity and stability of Pt NPs when hydrogen-treated TiO_2 nanotube was used as the catalyst support for PEMFCs, owing to the SMSI and enhanced electronic conductivity.[38] To the best of our knowledge, there is no report so far on studying the effect of the defective hydrogenated TiO_2 for MOR in DMFC applications.

Another approach to mitigating the low electronic conductivity of TiO_2 is to make it as a hybrid structure with highly conductive carbon materials. The morphology of the metal oxide in the hybrid support has a significant effect on the electrochemical performance of catalysts.[10] Amid the various morphologies (such as NPs, nanotubes, nanoarrays) of TiO_2 that have been studied as the catalyst supports, ultrathin-films or nanocoating on carbon supports attracted special attention due to the SMSI and maximal −OH groups that it can provide to the PGM NPs. In addition, they can provide a continuous electron conductive network, mimic the high surface area of underlying carbon support for better NP dispersion while effectively protecting the underlying carbon from corrosion.[10,31] Until today, only a few vacuum-based and/or energy-intensive methods have been reported for TiO_2 thin-film synthesis/deposition, such as atomic layer deposition (ALD),[39] chemical vapor deposition (CVD),[40] and hydrothermal/solvothermal methods.[41,42] Microwave-assisted synthesis has attracted a lot of attention due to its low cost, facile, rapid, and scalable nature.[43] In addition, since carbon materials have a higher microwave absorptivity than the solvent (as reflected in its high dielectric tangent loss values), the "specific heating" by microwave irradiation can be used to enable preferential TiO_2 nucleation and thin film growth on the carbon support, unlike the presence of large bulk reaction in conventional synthesis methods.[44] Manthiram et al. and Vigil et al. reported TiO_2 thin film deposition from solution on conductive ITO substrate using the microwave-assisted method at a relatively low temperature 150 °C when compared to those used in conventional TiO_2 synthesis.[44,45] However, deposition of TiO_2 as thin-films or core−shell structures on carbon supports using microwaves has not been explored for developing MOR electrocatalysts.

Herein, we report the microwave-assisted deposition of a conformal ultrathin TiO_2 film (or shell) on oxygen functionalized N-doped carbon nanotubes (ONCNT), to form a core−shell hybrid support for PtRu alloy NPs to enhance the MOR activity and stability. The PtRu NPs were also deposited on TiO_2/ONCNT support by the rapid microwave-assisted synthesis followed by a post-deposition thermal annealing process at 400 °C in a reducing atmosphere (3% H_2/97% Ar). Crystalline PtRu alloy NPs anchored on the defective hydrogenated ultrathin TiO_2 shell, named as PtRu/TiO_2/ONCNT-400, have been obtained. The as-prepared PtRu/TiO_2/ONCNT-400 catalyst exhibited enhanced CO oxidation kinetics, superior MOR activity, and excellent stability when compared to two types of benchmark commercial PtRu/C catalysts from Johnson Matthey (JM) and Tanaka KiKinzoku (TKK), respectively. We illustrate that this is attributed to the SMSI, continuous electron conductive network, and the increased hydroxyl groups provided by the ultrathin defective hydrogenated TiO_2 coating on the ONCNT. The systematical material and electrochemical characterizations reveal that the SMSI between the PGM catalyst and TiO_2 coating is critical in reducing the CO poisoning on Pt sites by enhancing the CO oxidation kinetics via stronger OH^- adsorption and abundant −OH groups on the underlying TiO_2 surface. Such multifunc-

https://doi.org/10.1021/acsanm.1c03742
ACS Appl. Nano Mater. 2022, 5, 3275−3288

tional hybrid MOR catalysts can be synthesized in a scalable process for future DMFCs.

2. EXPERIMENTAL SECTION

2.1. Chemicals and Materials. The potassium hexachloroplatinate (K_2PtCl_6), ruthenium chloride ($RuCl_3{\cdot}xH_2O$), and Nafion solution (5 wt % in lower aliphatic alcohols) were purchased from Sigma-Aldrich (St. Louis, MO). The titanium tetraisopropoxide (TTIP), ethylene glycol (EG), sulfuric acid (H_2SO_4), nitric acid (HNO_3), pure ethanol 200 proof, and methanol (ACS grade) were purchased from Fisher Scientific (Hampton, NH). Ultrapure water (18.2 MΩ.cm at 25 °C) purified from a Millipore water system (EASYPURE II, Thermo Scientific, Waltham, MA) was used to prepare all aqueous solutions for the experiments. The commercial Pt/C catalyst (20 wt % Pt on carbon, HiSPEC 3000) and PtRu/C catalyst (48.0 wt % Pt and 23.1 wt % Ru on carbon, HiSPEC 12100) by Johnson Matthey (JM) were purchased from Alfa Aesar (Tewksbury, MA) as the benchmark reference. Another benchmark commercial PtRu/C catalyst (TEC 66E50−32.8 wt % Pt and 16.9 wt % Ru on carbon) was purchased from Tanaka Kikinzoku International (America) Inc. (Schaumburg, IL), referred as TKK.

2.2. Material Synthesis. *2.2.1. Preparation of NCNTs.* N-doped CNTs (NCNTs) were synthesized from the pristine CNTs (obtained from Zhongshan CNM Plastic Co., Ltd., Zhongshan, China) by chemical vapor deposition of pyridine on the cleaned pristine CNTs. Briefly, CNT was placed into a quartz tube and heated from room temperature to 760 °C at a rate of 10 °C/min under N_2 atmosphere. Pyridine solution was charged into the quartz tube at 2 mL/h for 4 h. After that, the furnace was cooled down in N_2 atmosphere and NCNT was obtained.

2.2.2. Preparation of TiO_2/ONCNT. The NCNT was first oxygenated by treating 1.0 g of NCNT in an aqueous mixture of 2.0 M H_2SO_4 and 4.0 M HNO_3 at 120 °C for 12 h under constant stirring. The obtained oxygenated NCNT (ONCNT) was washed with ultrapure water until the pH reached 7.0, filtered, and dried at 80 °C in a vacuum oven. Then, 10.0 mg of ONCNT was dispersed in 6.0 mL of ethanol by ultrasonication for 30 min. Further, 10.0 mg of TTIP was added to this dispersion and sonicated in a water bath. After 30 min sonication, this mixture was transferred to a 10 mL Pyrex glass microwave vessel and put into DiscoverSP microwave synthesizer (CEM Corporation., Matthews, NC). A microwave irradiation was applied in the dynamic mode with the power up to 300 W to maintain a reaction temperature of 150 °C for 5 min. The reaction pressure rose to ∼19 bar during the process. After reaction, the naturally cooled product mixture was washed 2−3 times using ethanol to remove the unreacted precursors. The solid materials were collected by centrifugation and dried at 80 °C in a vacuum oven to obtain the TiO_2-coated ONCNTs, referred as TiO_2/ONCNT.

2.2.3. Preparation of PtRu/TiO_2/ONCNT-400. To deposit PtRu catalysts, 12.5 mg of K_2PtCl_6, 5.1 mg of $RuCl_3{\cdot}xH_2O$, and 16.0 mg of TiO_2/ONCNT were dispersed in 20 mL of mixture of ethylene glycol and water (at 4:1 volume ratio) by ultrasonication for 1 h. The solution was then transferred to 35 mL Pyrex glass microwave vessel. The weight ratio of Pt and Ru is maintained at 2:1 in the precursors. Ethylene glycol serves as a reducing agent and solvent in this reaction. The mixture was irradiated with a 300 W microwave under the dynamic mode to maintain a reaction temperature of 190 °C for 20 min in DiscoverSP microwave synthesizer to deposit Pt and Ru NPs onto TiO_2/ONCNT. The reaction pressure rose to ∼8 bar during this process. The cooled product mixture was washed several times using acetone to remove residual ethylene glycol. The solid materials were collected by centrifugation and then dried at 80 °C in a vacuum oven to obtain PtRu/TiO_2/ONCNT. The dried catalyst material was annealed in a tube furnace at 400 °C for 2 h in 3% H_2/97% Ar atmosphere at a ramp rate of 10 °C/min, to form crystalline PtRu alloyed NPs and defective hydrogenated TiO_2 shell on the ONCNT. The as-prepared catalyst is named as PtRu/TiO_2/ONCNT-400. Synthesis of control samples was carried out using the same reaction conditions as mentioned above with appropriate precursors but skipping some specific intermediate steps.

2.3. Material Characterization. The structure of the catalysts was characterized using three transmission electron microscopes (TEM) at different stages of the project, including a Tecnai Osiris Scanning/Transmission Electron Microscope (S/TEM, FEI, Hillsboro, OR) at a 200 kV acceleration voltage, a Hitachi H-8100 TEM (Hitachi, Krefeld, Germany) at a 200 kV acceleration voltage and a Philips CM 100 TEM at a 100 kV acceleration voltage. The crystal structure of the catalysts was examined using Bruker AXS D8 Advance Discover Diffractometer (Bruker Corporation, Karlsruhe, Germany) with a Cu Kα radiation of wavelength 0.15418 nm and a detector slit width of 1 mm. XRD reference spectra are used from Joint Committee on Powder Diffraction Standards (JCPDS). The composition of the catalysts was determined using a Thermogravimetric Analyzer (TGA) Q50 system (TA Instruments—Waters LLC, New Castle, DC) from the room temperature to 900 °C in an air atmosphere. The surface chemical composition of the catalysts was characterized using a PHI 5000 Versa XPS system (Chanhassen, MN) with a monochromatized Al Kα source (1486.7 eV). All the XPS spectra were obtained using a 400 μm spot size. Shirley background was used in the curve fitting. The binding energy (B.E.) of all XPS data was calibrated vs the standard sp^2 C 1s peak at 284.60 eV.

2.4. Electrochemical Measurements. All the half-cell electrochemical experiments were performed in a standard three-electrode setup using a CHI 760D electrochemical workstation (CH Instruments, Austin, TX) at room temperature. A silver−silver chloride (Ag/AgCl in 1.0 M KCl) reference electrode and a coiled Pt counter electrode (0.55 mm in diameter and 23 cm in length) were used. The working electrode was prepared by drop-casting the catalyst ink onto a glassy carbon electrode (GCE) encased in a PEEK rod. Before drop-casting the catalyst ink, the GCE was polished using 0.05 μm alumina slurry. The catalyst ink was prepared by dispersing the required amount of catalyst powder in 1.0 mL of mixture of ethanol and ultrapure water (at 3:1 volume ratio) with addition of the 30 μL of Nafion solution (5 wt % in lower aliphatic alcohols). The loading of the platinum group metal (PGM, specifically Pt and Ru in this study) was maintained at 54 $\mu g/cm^2$ for all catalysts in the half-cell studies. Before studying the MOR catalytic activity, the catalyst-coated electrodes were subjected to activation by cyclic voltammetry (CV) in the potential range of −0.2 to 0.8 V vs Ag/AgCl (1.0 M KCl) at a sweep rate of 100 mV/s for 50 cycles in Ar-purged 0.50 M H_2SO_4 electrolyte. The MOR experiments were performed by recording CV in the potential range of −0.2 to 0.8 V vs Ag/AgCl (1.0 M KCl) at a scan rate of 50 mV/s for 500 cycles in Ar-purged 0.5 M H_2SO_4 solution containing 0.75 M methanol. The CV curves of the 100th cycle was chosen to compare the MOR activity of various catalysts in this paper unless otherwise specified. For direct comparison of the potentials with literature, the measured electrode potential vs the Ag/AgCl (1.0 M KCl) reference electrode is converted to the value vs the reversible hydrogen electrode (RHE) using the following equation:

$$E_{(\text{vs RHE})} = E_{(\text{vs Ag/AgCl})} + E_{(\text{Ag/AgCl vs SHE})} + 0.059\text{pH} = E_{(\text{vs Ag/AgCl})} + 0.222\text{V} \quad (1)$$

where $E_{(\text{vs Ag/AgCl})}$ is the measured potential vs the Ag/AgCl (1.0 M KCl) reference electrode, $E_{(\text{Ag/AgCl vs SHE})}$ = 0.222 V is the Ag/AgCl (1.0 M KCl) reference electrode potential vs SHE, and pH = 0 for 0.50 M H_2SO_4.

The CO stripping voltammetry experiments were performed in 0.50 M H_2SO_4 to evaluate the catalyst activity toward CO oxidation and to determine the active electrochemical surface area (ECSA) of the catalyst. In CO stripping experiments, the electrolyte was first purged with Ar gas to remove any dissolved oxygen species in the electrolyte. Then, a pure CO gas was used to purge the electrolyte for 10 min while the potential of the working electrode was held at 0.10 V vs RHE. After 10 min, the purging gas was switched back to pure Ar to purge for 30 min to remove the dissolved CO gas from the electrolyte, while the potential of the working electrode was still held at 0.10 V vs RHE which retained the adsorbed CO monolayer on the

https://doi.org/10.1021/acsanm.1c03742
ACS Appl. Nano Mater. 2022, 5, 3275−3288

Scheme 1. Synthesis Process for PtRu/TiO_2/ONCNT-400

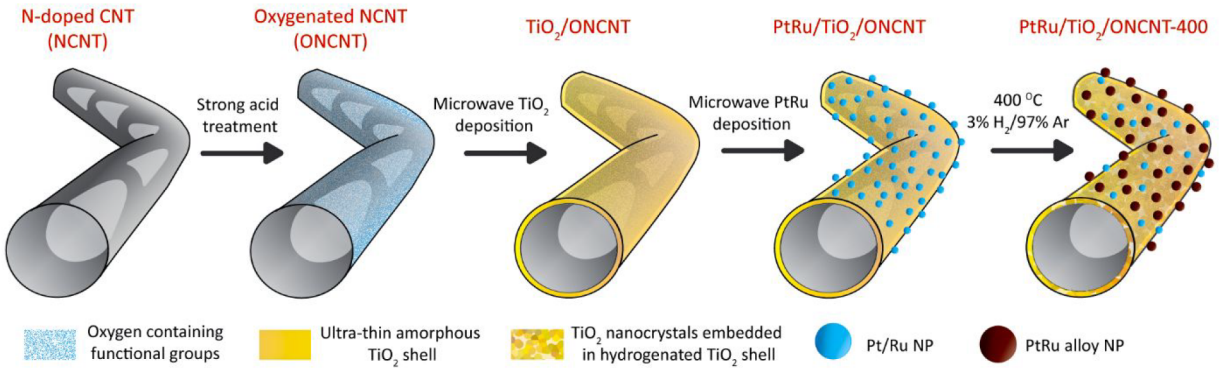

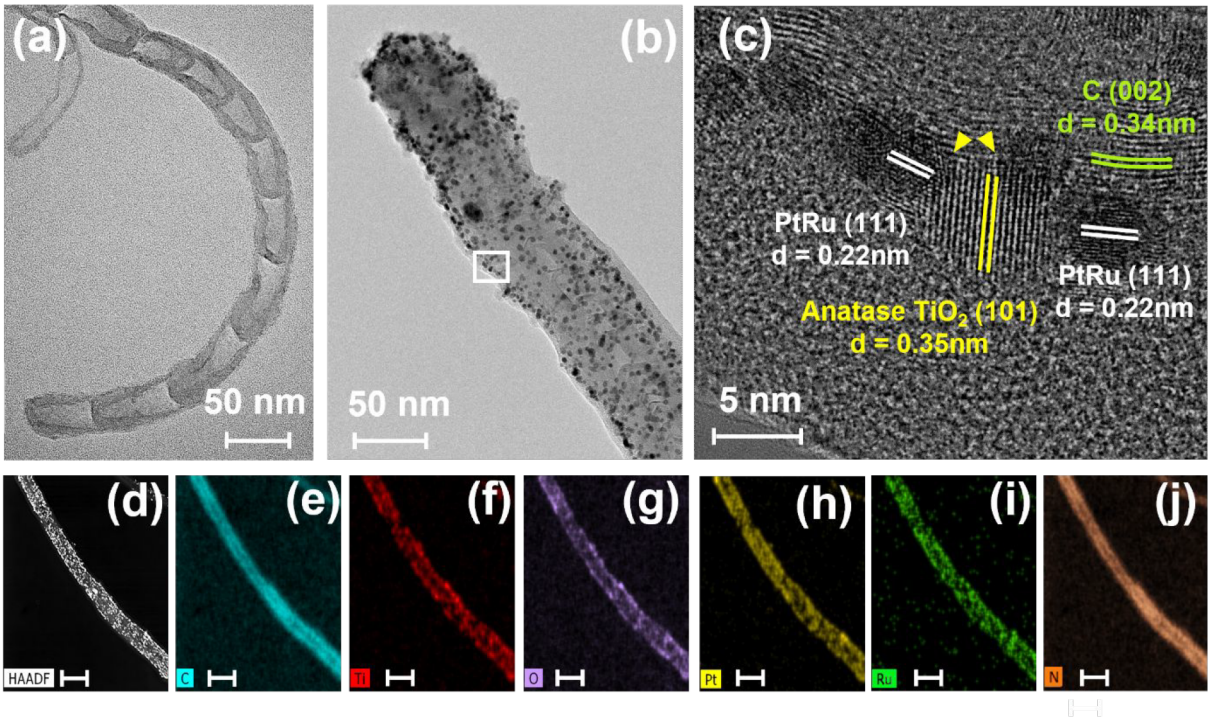

Figure 1. (a) TEM image of TiO_2/ONCNT. (b) TEM image of PtRu/TiO_2/ONCNT-400. (c) High-resolution TEM (HRTEM) image of the rectangular portion of panel (b) with the lattice fringes corresponding to C(002), anatase TiO_2(101), and PtRu(111). (d) HAADF-STEM image and (e–j) STEM-EDX elemental mapping of C, Ti, O, Pt, Ru, and N in PtRu/TiO_2/ONCNT-400. The scale bar in the (d–j) is 100 nm.

Pt surface. Subsequently, the CO monolayer on the Pt surface was stripped off with a linear anodic sweep at 10 mV/s from 0.10 to 1.222 V vs RHE. A few CV cycles were taken following CO stripping to evaluate the baseline of the electrode.

The ECSA of Pt in the catalysts was determined using the following equation:

$$\mathrm{ECSA} = \frac{Q_a}{Q_{CO}^{0} \times m_{Pt}} \quad (2)$$

where Q_a ($\mu C/cm^2$) is the charge associated with the integrated area of CO oxidation peak; Q_{co}^{0} = 420 $\mu C/cm^2$ is the charge required to oxidize a monolayer of CO adsorbed on 1 cm^2 of flat Pt surface, and m_{Pt} (g_{Pt}/cm^2) is the mass loading of Pt on the working electrode surface.

3. RESULTS AND DISCUSSION

The process to synthesize the PtRu/TiO_2/ONCNT-400 catalyst is illustrated in Scheme 1 and is detailed in the Experimental Section. The final catalyst as well as the control samples are carefully characterized to reveal the structure and properties. The key features obtained at each step are highlighted.

3.1. Morphology of the Catalysts by TEM. Figure S1 of the Supporting Information (SI) shows the low-magnification TEM images of the as-prepared PtRu/TiO_2/ONCNT-400 and two benchmark commercial PtRu/C catalysts (JM and TKK). The catalyst support used in this study, i.e., NCNT, has a long fiber-like structure with the diameter ranging from 20–40 nm and the length ranging from 2–10 μm. This is drastically different from the amorphous carbon support of ~30–50 nm diameter spherical NPs in the two state-of-the-art commercial PtRu/C catalysts.

In addition, the NCNT catalyst support shows a characteristic bamboo-like graphitic internal structure which consists of stacks of conical graphitic layers along the fiber axis. This unique structure presents abundant electrochemically active graphitic edge sites at the sidewall which are expected to have stronger interaction with metal oxides and PGM NPs. More

https://doi.org/10.1021/acsanm.1c03742
ACS Appl. Nano Mater. 2022, 5, 3275–3288

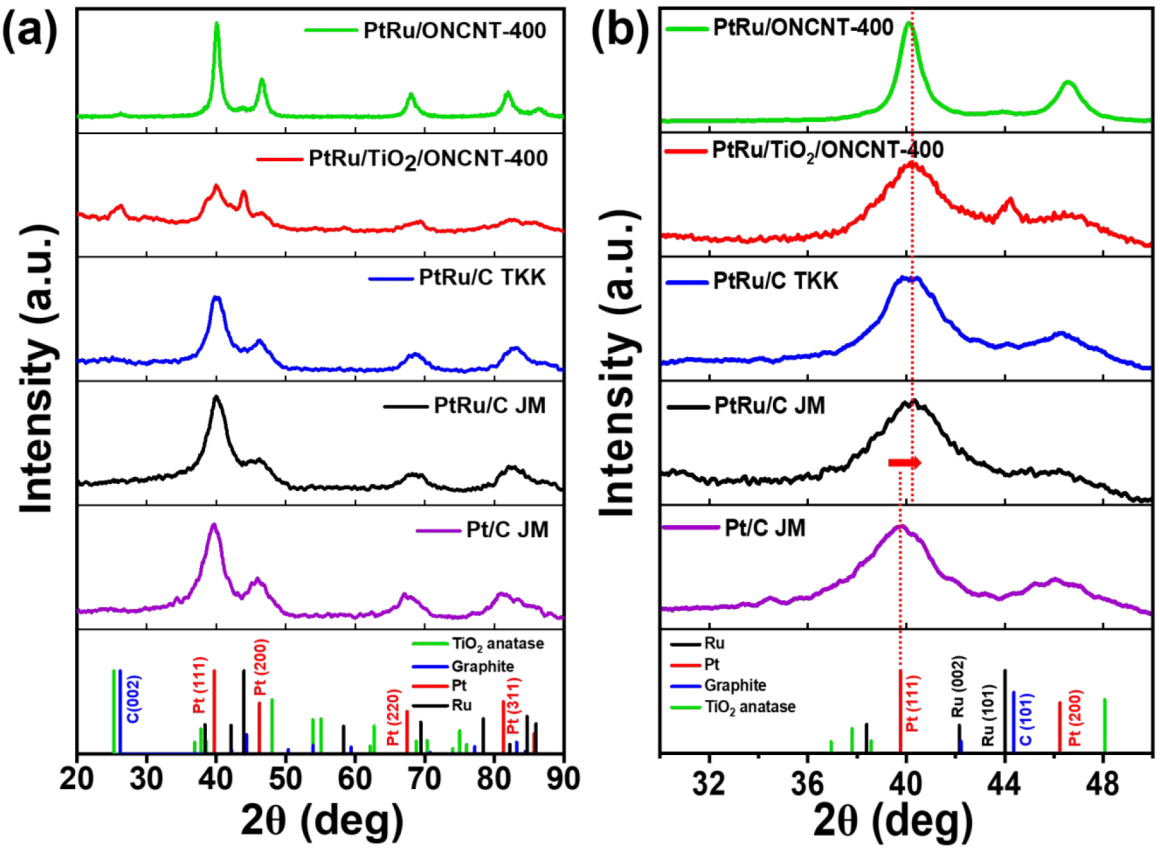

Figure 2. XRD patterns (a) in the full 2θ range of 20° to 90° and (b) in the narrower 2θ range of 30° to 50° of TiO_2 anatase (JCPDS# 21−1272), graphite reference (JCPDS# 75−1621), Pt reference (JCPDS# 04−0802), and Ru reference (JCPDS # 06−0663) compared with Pt/C JM, PtRu/C JM, PtRu/C TKK, PtRu/TiO_2/ONCNT-400, and PtRu/ONCNT-400.

details of the internal conically stacked graphitic structure of the NCNT are illustrated with the high-magnification TEM image in Figure S2a. As NCNTs are hydrophobic, they tend to aggregate and are not easy to form a stable well-dispersed solution. This was improved by treating it with strong acids to incorporate oxygenated functional groups at the graphitic edges along the sidewall. The resulting hydrophilic ONCNT (Figure S2b) enabled uniform dispersion in aqueous solutions for subsequent reactions. After microwave-assisted deposition, an ultrathin conformal TiO_2 shell was formed on the ONCNT core, making it a TiO_2/ONCNT hybrid material as shown by the TEM image in Figure 1a. As will be discussed later, the as-deposited TiO_2 shell is a disordered amorphous material. Thus, the TEM contrast between TiO_2 and ONCNT was quite low and inadequate to clearly reveal the interface. However, after thermal annealing the as-produced TiO_2/ONCNT at 400 °C for 2 h in 3% H_2/97% Ar atmosphere, denoted as TiO_2/ONCNT-400, the contrast was improved, and a clear core−shell structure can be observed by TEM in Figure S2c, with the TiO_2 shell thickness about 5 nm.

The TiO_2 shell was found to efficiently improve the nucleation and anchoring of Pt or PtRu NPs in the subsequent microwave process for PGM catalyst deposition. As shown in Figure 1b, uniform and well-separated PtRu NPs are retained on the surface of TiO_2/ONCNT support after post-PGM-deposition thermal annealing at 400 °C for 2 h in 3% H_2/97% Ar atmosphere, denoted as PtRu/TiO_2/ONCNT-400. The average particle size was found to be 3.8 ± 0.6 nm as shown in the histogram in Figure S3. This is in the right range for highly active PGM catalysts. The nature of the TiO_2 shell and PtRu NPs in PtRu/TiO_2/ONCNT-400 is clearly illustrated in the high-resolution TEM image in Figure 1c. The lattice fringes match that for anatase TiO_2 (101), PtRu (111) and C (002), respectively. It confirms that the crystalline PtRu catalyst NPs are anchored on the surface of a TiO_2 shell consisting of anatase TiO_2 nanocrystals (about 5 to 8 nm in dia.) embedded in a continuous amorphous TiO_2 film. The yellow arrows highlight the region where the PtRu NPs are in direct contact with the crystalline TiO_2 support. The HAADF-STEM elemental mapping of PtRu/TiO_2/ONCNT-400 (shown in Figures 1d−j) further confirms the presence and uniform distribution of C, Ti, O, Pt, Ru, and N elements. It is to be noted that the diameter of the ONCNT is increased in Ti and O mapping (see Figure 1f,g) when compared to C mapping (Figure 1e), depicting the formation of TiO_2 shell around the ONCNT. This further reveals that the average thickness of the TiO_2 shell is ∼5 nm. Comparing Figures 1d−j with the HAADF-STEM elemental mapping of TiO_2/ONCNT (before PtRu deposition) in Figures S4a−e, the microwave-assisted PtRu deposition and subsequent thermal annealing process did not change the morphology and distribution of C, Ti, O, and N in the TiO_2/ONCNT support.

Additional TEM images and NP size distribution histograms of Pt and PtRu catalysts deposited on three types of supports, including ONCNT, TiO_2/ONCNT, and TiO_2/ONCNT-400, are shown in Figures S5 and S6, denoted as Pt/ONCNT, Pt/TiO_2/ONCNT, Pt/TiO_2/ONCNT-400, PtRu/ONCNT, PtRu/TiO_2/ONCNT, and PtRu/TiO_2/ONCNT-400. The particle size distribution of these samples is quite similar, with the average size of ∼3.2 to 3.8 nm. In contrast, the

https://doi.org/10.1021/acsanm.1c03742
ACS Appl. Nano Mater. 2022, 5, 3275−3288

average size of PGM NPs increases to 4.8 ± 1.3 nm in Pt/ONCNT-400 (Figure S7a) and 5.4 ± 1.4 nm in PtRu/ONCNT-400 (Figure S7b), respectively, which do not have the TiO_2 coating. Clearly, the TiO_2 shell helps to prevent PtRu agglomeration during thermal annealing, presumably due to stronger PGM-TiO_2 interaction as reported in literature.[23,24,46]

3.2. Composition of the Catalysts by TGA. TGA analyses of PtRu/TiO_2/ONCNT-400 and its corresponding control samples were carried out in air atmosphere to determine the weight percentage (wt %) of each element or compound present in the catalyst, as shown in Figure S8a. In the temperature range of 440 to 640 °C, the control carbon support ONCNT-400, i.e., ONCNTs annealed at 400 °C in 3% H_2/97% Ar, is almost burnt out, leaving only ∼4% graphitic residue. In the TGA measurements, Ru atoms in the NPs are oxidized into RuO_x (with x = 1.20) in the range of 400 to 625 °C leading to increase of the weight to ∼119% as shown in the control Ru NPs (purple curve of Figure S8a). The weight of Pt and TiO_2 control samples remain nearly constant in the whole temperature range from room temperature to 900 °C. On the basis of these observations and reaction stoichiometry, the wt % of each component can be derived. Detailed explanations and calculations of TGA are given in the SI file. The wt % of Pt, Ru, TiO_2, and ONCNT in the PtRu/TiO_2/ONCNT-400 catalyst is found to be 25.5%, 10.2%, 20.4%, and 43.9%, respectively. The total PGM wt % is 35.7%.

The TGA curves of commercial PtRu/C catalysts from JM and TKK are compared with our PtRu/TiO_2/ONCNT-400 catalyst in Figure S8b. While all curves show decrease in the weight in a well-defined step function due to burning off carbon supports, the starting and ending temperatures of our PtRu/TiO_2/ONCNT-400 catalyst are more than 100 °C higher than those of the two commercial catalysts. The graphitic NCNT support is indeed more stable than the amorphous carbon supports in the commercial catalysts. The wt % in the stabilized region above 600 °C are 78.9% for the PtRu/C JM and 55.6% for the PtRu/C TKK. By applying the above TGA analysis method to the commercial PtRu/C catalysts, the derived PtRu wt % are 73.2% (JM) and 50.6% (TKK), which are within ∼1 to 2% from the vendor specified values of 71.1% (JM) and 49.7% (TKK) (see details in the SI file). This validates the reliability of TGA in determining the wt % of individual components in the catalyst and support.

3.3. Crystal Structure of the Catalysts by XRD. The as-deposited PtRu catalysts by the microwave process were found to be disordered. Thermal annealing at 400 °C in 3% H_2/97% Ar was applied to convert them into crystalline PtRu alloys. XRD analysis was carried out to understand the crystal structure of the catalysts as shown in Figures 2 and S9. The diffraction peaks of the PtRu/TiO_2/ONCNT-400 at 2θ angles of 26.1°, 40.3°, 44.2°, 46.72°, 68.4°, and 82.8° are indexed as C(002), Pt(111), Ru(101), Pt(200), Pt(220), and Pt(311), respectively. In expanded plots in Figure 2b, the Pt(111) peak of thermal annealed PtRu catalysts, i.e., PtRu/ONCNT-400 and PtRu/TiO_2/ONCNT-400 shifts slightly to higher 2θ angles compared to 2θ = 39.76° in PtRu/TiO_2/ONCNT (before annealing, see Figure S10) and Pt reference spectrum (JCPDS: 04−0802).[47] A similar peak shift is observed in both JM and TKK commercial PtRu/C catalysts compared to Pt/C from JM. The shift to higher 2θ angles reveals the successful incorporation of Ru atoms into the Pt lattice to form a crystalline PtRu alloy with a contracted lattice since the atomic radius of Ru is smaller than Pt.[48] The atomic fraction of Pt and Ru in the PtRu alloy in PtRu/TiO_2/ONCNT-400 can be calculated as 1.6:1 using Vegard's law,[49,50] as described in the SI file. The average crystallite size of PtRu alloy NPs is estimated to be 3.2 nm in PtRu/TiO_2/ONCNT-400 and 5.6 nm in PtRu/ONCNTs-400 using the Scherrer's formula:[51]

$$D = K\lambda/\beta\cos\theta \quad (3)$$

where D is the crystallite size, K is the shape factor (0.89), λ is the X-ray source wavelength (1.5418 Å for Cu Kα radiation), β is the full width at half-maximum of the diffraction peak (in radians), and θ is the half of the 2θ angle of the diffraction peak. The resulting values are close to the average particle size measured with TEM, which further reveals that TiO_2 coating is critical in confining PtRu NPs on the surface and preventing their agglomeration during the thermal annealing.

Figure S9b shows that Pt(220) diffractions also shift to higher 2θ angles after forming PtRu alloy in the annealed samples and the two PtRu/C commercial catalysts. In contrast, the XRD patterns of the bare supports, including TiO_2/ONCNT and TiO_2/ONCNT-400 (see Figure S9c), only show a clear C(002) peak and a very weak C(101) peak. It is to be noted that the diffraction peaks for anatase TiO_2 were not observed [when compared to TiO_2 anatase (JCPDS: 21−1272) reference spectra] in any of the TiO_2-coated ONCNT samples, which could be due to the dominance of the defective disordered nature of the TiO_2 coating. Only a small amount of TiO_2 anatase nanocrystals are embedded in the amorphous shell as shown in the HRTEM image in Figure 1c. Furthermore, the XRD patterns of Pt/ONCNT, Ru/ONCNT, and PtRu/ONCNT in Figure S9c reveal that Pt and Ru form separate nanocrystals matching the standard reference spectra of Pt (JCPDS: 04−0802) and Ru (JCPDS: 06−0663). XRD results provide further evidence that thermal annealing is essential for forming crystalline PtRu alloy NPs that are required for high catalytic activities, while the TiO_2 coating on the carbon support, though in a disordered form, is effective in anchoring the PGM NPs during thermal annealing to prevent agglomeration.

3.4. Chemical Analyses of the Catalysts by XPS. The strong PGM-TiO_2 interaction and the surface chemical composition of all catalysts were investigated by XPS. Figure S11 shows the XPS survey spectra of the catalysts. The at% of each element calculated from the survey spectra are summarized in Table S1. The surface atomic nitrogen content in NCNT and ONCNT was found to be ∼9 at% and ∼10 at%, respectively, which confirms the high nitrogen-doping in the pristine NCNT and oxygenated NCNT (ONCNT). The surface oxygen content in ONCNT (16 at%) was slightly higher than in the pristine NCNT (15 at%).

The high-resolution spectra of C 1s, N 1s, and O 1s were first collected from NCNT and ONCNT to investigate the surface chemical environment changes before and after strong acid treatment. The C 1s of NCNT and ONCNT were deconvoluted into six components with binding energies (BEs) of 284.60, 285.12, 286.20, 287.35, 289.03, and 291.10 eV, as shown in Figure S12a. It is dominated by the sp^2 hybridized carbon atoms at 284.60 eV with a much smaller content of sp^3 hybridized carbon atoms in the NCNT planes.[52,53] The peaks at 285.12, 286.20, 287.35, 289.03, and 291.10 eV correspond to sp^3 hybridized C atoms, C−O/C−N, C═O, and O−C═O bonds and π−π* of the shakeup satellite peak from sp^2 C,[53] respectively. C−N bond at 285.12 eV further validates the nitrogen doping in NCNT. Similarly, the O 1s of NCNT and

https://doi.org/10.1021/acsanm.1c03742
ACS Appl. Nano Mater. 2022, 5, 3275−3288

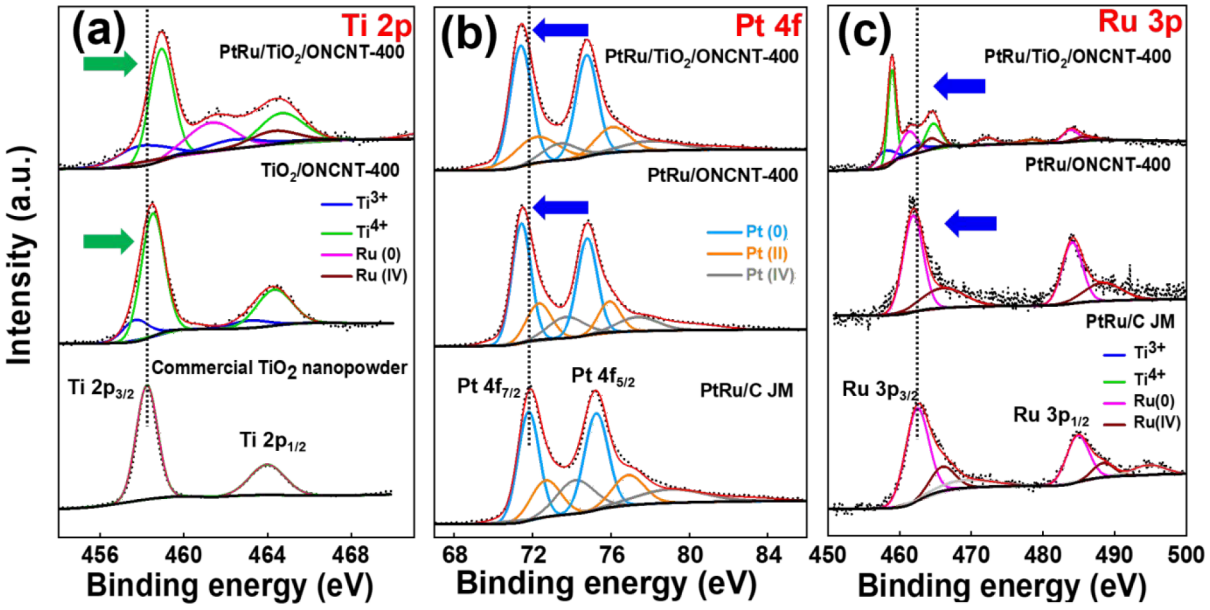

Figure 3. XPS analysis of (a) Ti 2p spectra of commercial TiO_2 nano powder, TiO_2/ONCNT-400, and PtRu/TiO_2/ONCNT-400; (b) Pt 4f spectra of commercial PtRu/C JM, PtRu/ONCNT-400, and PtRu/TiO_2/ONCNT-400; and (c) Ru 3p spectra of commercial PtRu/C JM, PtRu/ONCNT-400, and PtRu/TiO_2/ONCNT-400. The legends in each panel apply to all three curves in that panel.

ONCNT were deconvoluted into three components with BEs of 531.23, 532.10, and 533.57 eV corresponding to carboxylic O−C═O group, C−O group, and hydroxyl C−OH bonds,[54] respectively, as shown in Figure S12b. The N 1s of NCNT and ONCNT were deconvoluted into five components with BEs of 398.57, 400.00, 401.20, 403.32, and 405.19 eV, which correspond to pyridinic N, pyrrolic N, graphitic N, pyridinic-N-oxide and C−O−N,[54,55] respectively, as shown in Figure S12c. Table S2 summarizes and compares the relative at% of each component of deconvoluted peaks in C 1s, O 1s, and N 1s of NCNT and ONCNT. With strong acid functionalization, some sp^3 carbon has converted to C−O, C═O, and O−C═O, showing an increase in the relative at% of carbonyl and carboxyl groups in ONCNT when compared to NCNT. Similarly, some of the O−C═O was transformed to C−O (~7.2 at%) and −OH (~3.2 at%) groups in O 1s of ONCNT when compared to the C−O (~4.2 at%) and −OH (~2.2 at%) in NCNT. The increase of carboxyl and carbonyl groups at the edge sites of ONCNT can promote the TiO_2 deposition in the subsequent process.[20,56,57]

The chemical composition of the TiO_2 coating on ONCNT is illustrated in the high-resolution Ti 2p XPS spectra in Figure S13a. As a reference, the Ti 2p spectra of the commercial TiO_2 anatase nanopowder can be deconvoluted into a pair of peaks at 458.23 and 463.98 eV, respectively, corresponding to the Ti $2p_{3/2}$ and Ti $2p_{1/2}$ doublet of Ti^{4+} ions in TiO_2. Whereas for TiO_2/ONCNT, another pair of peaks (about 12.2 at%) at lower BE needs to be included to fit the Ti 2p spectra, which is due to the Ti^{3+} ions in TiO_2. Some of the Ti^{4+} was reduced into Ti^{3+} during the microwave-assisted deposition. In TiO_2/ONCNT-400, the Ti^{3+} composition increased to ~16.7 at% (see Figure S13b) due to H_2 reduction during the thermal annealing, reflecting the formation of defective hydrogenated TiO_2.[58−60] It is noteworthy that, for electrocatalysis, the defective hydrogenated TiO_2 is beneficial due to the higher electronic conductivity than the pristine TiO_2 anatase.[35,61,62]

The interaction of PtRu catalyst with the TiO_2 support can be derived by comparing the high-resolution XPS spectra of Ti 2p, Pt 4f, and Ru 3p peaks of PtRu/TiO_2/ONCNT-400 with those of PtRu/ONCNT-400 and other control samples including TiO_2/ONCNT-400, commercial TiO_2 anatase nanopowder and PtRu/C JM catalyst, as shown in Figure 3. The BE and relative at% of each deconvoluted peak are shown in Table S3. Figure 3a shows that the Ti^{3+} content in PtRu/TiO_2/ONCNT-400 further increases to ~27.0 at% from ~16.7 at% in TiO_2/ONCNT-400. In addition, the BE of $2p_{3/2}$ peak of Ti^{4+} in PtRu/TiO_2/ONCNT-400 shifts up to 458.92 eV compared to that in TiO_2/ONCNTs-400 (458.50 eV) and commercial TiO_2 anatase nanopowder (458.32 eV), suggesting a lower electron density at Ti^{4+} sites likely due to electron transfer from Ti^{4+} to PtRu in PtRu/TiO_2/ONCNT-400 catalyst. It is to be noted that the Ti 2p doublets of Ti^{4+} and Ti^{3+} states in PtRu/TiO_2/ONCNT-400 partially overlap with the Ru $3p_{3/2}$ peaks (at BE of 458.92 and 458.02 eV). Nevertheless, they can be separated by deconvolution.

Figure 3b shows that the Pt 4f spectra of PtRu/TiO_2/ONCNT-400, PtRu/ONCNT-400 (the control w/o TiO_2), and the commercial PtRu/C JM catalyst can all be deconvoluted into three pairs of Pt $4f_{7/2}$ and Pt $4f_{5/2}$ doublets attributed to Pt(0), Pt^{2+}, and Pt^{4+} states in metallic, PtO and $Pt(OH)_2$, and PtO_2 species,[63] respectively. Pt (0) is the dominant species consisting of ~61% of Pt atoms, which is higher than ~51% in PtRu/C JM catalyst. The BE of Pt $4f_{7/2}$ of metallic Pt in PtRu/TiO_2/ONCNT-400 downshifted to 71.41 eV from 71.47 eV in PtRu/ONCNT-400 and 71.82 eV in the commercial PtRu/C JM catalyst. This trend is opposite to that of the Ti 2p peaks, indicating a higher electron density at Pt atomic sites in PtRu/TiO_2/ONCNT-400 due to partial electron transfer from Ti^{4+} to Pt. In Figure 3c, the Ru 3p peak of PtRu/TiO_2/ONCNT-400, PtRu/ONCNT-400, and commercial PtRu/C JM catalysts can all be deconvoluted into two pairs of doublets, corresponding to Ru(0) and Ru^{4+} in metallic and RuO_2 species,[64] respectively. Ru(0) comprises of as high as ~69% of all Ru atoms in PtRu/TiO_2/ONCNT-400, again higher than ~64% in PtRu/C JM catalyst. The BE of Ru $3p_{3/2}$ of metallic Ru in the three samples shows the similar

https://doi.org/10.1021/acsanm.1c03742
ACS Appl. Nano Mater. 2022, 5, 3275−3288

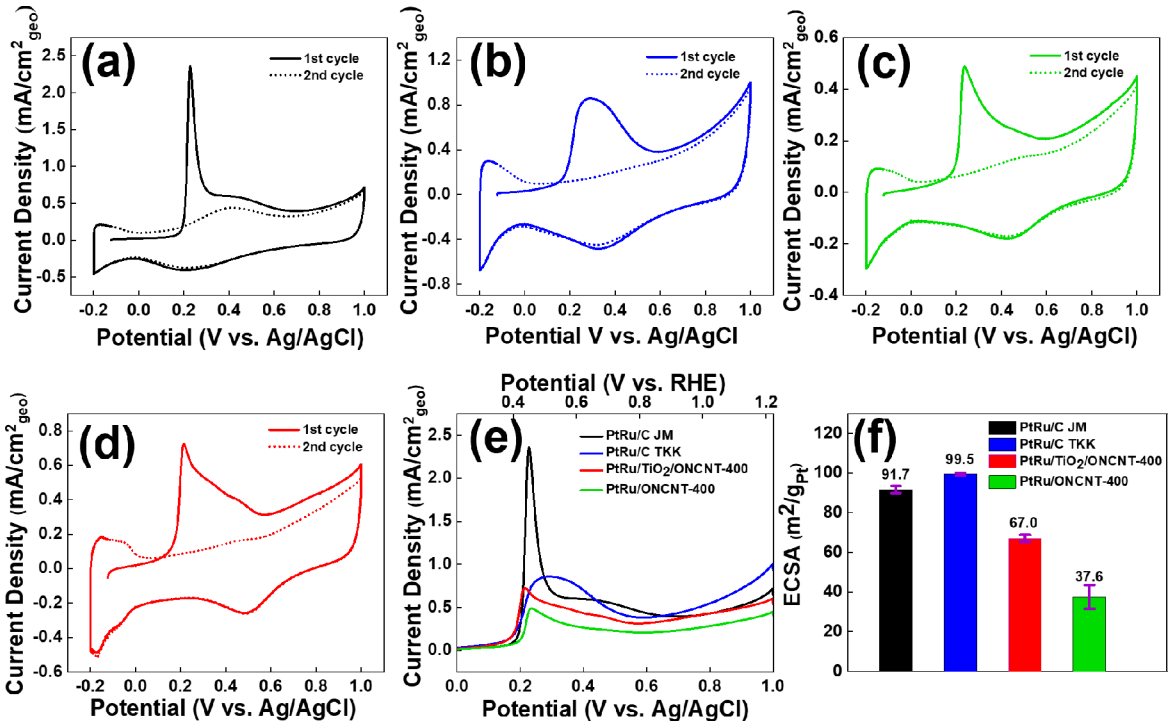

Figure 4. CO stripping voltammograms of (a) commercial PtRu/C JM; (b) commercial PtRu/C TKK; (c) PtRu/ONCNT-400; and (d) PtRu/TiO_2/ONCNT-400 catalysts recorded in Ar-purged 0.50 M H_2SO_4 solution at a scan rate of 10 mV/s. (e) Comparison of first anodic scan of CO stripping curves of PtRu/ONCNT-400 and PtRu/TiO_2/ONCNT-400 in comparison with the commercial PtRu/C catalysts from TKK and JM. (f) Bar plot of ECSA of different catalysts derived from the CO stripping measurements. The filling solution of Ag/AgCl reference electrode is 1.0 M KCl.

downshift trend as Pt 4f peaks in Figure 3b, with the lowest value in PtRu/TiO_2/ONCNT-400 (461.32 eV) comparing to PtRu/ONCNT-400 (461.87 eV) and PtRu/C JM (462.43 eV). This indicates that electron transfer also occurs from Ti^{4+} to Ru sites. Overall, the XPS spectra in Figure 3 depict that there is likely a partial electron transfer from Ti^{4+} sites to the metallic Pt and Ru sites, resulting in a SMSI between the PtRu NP and TiO_2 support. This downshift in Pt 4f BE will give a stronger Pt-CO binding, but it has an even bigger effect in increasing the OH^- binding on Pt which was found to accelerate the oxidation of CO to CO_2 and enhance C−H cleavage on Pt sites to improve MOR kinetics.[19]

3.5. Assessment of CO Oxidation with Anodic CO Stripping. As CO is a strong intermediate which poisons the Pt sites during MOR, it is important to investigate the anti-CO poisoning ability of a prepared catalyst. Linear CO stripping voltammograms and the consequent CV curves are present in Figures 4a−d to evaluate the ability of CO oxidation and derive the ECSA of the optimal PtRu/TiO_2/ONCNT-400 catalyst in comparison with PtRu/ONCNT-400 and the commercial PtRu/C catalysts from JM and TKK. All measurements were done in 0.50 M H_2SO_4 at a PGM catalyst loading of 54 $\mu g/cm^2$. All catalysts show a clear anodic stripping peak in the first positive scan due to electro-oxidation of the pre-adsorbed CO on the Pt surface. All subsequent CV curves except the PtRu/C JM catalyst show only the flat baseline confirming the complete stripping of adsorbed CO. Figure 4e compares the first anodic CO stripping curve of the four catalysts.

The CO oxidation onset potential for all catalysts is determined when the oxidation current reaches 0.150 mA/cm^2_{geo} and summarized in Table S4. The obtained CO oxidation onset potential increases in the order of PtRu/TiO_2/ONCNT-400 (~0.170 V), PtRu/C TKK (~0.170 V), PtRu/C JM (~0.190 V), and PtRu/ONCNT-400 (~0.205 V), versus an Ag/AgCl (1.0 M KCl) reference electrode. The CO oxidation peak potential appears in a different increasing order of PtRu/TiO_2/ONCNT-400 (~0.214 V), PtRu/C JM (~0.228 V), PtRu/ONCNT-400 (~0.234 V), and PtRu/C TKK (0.302 V), versus an Ag/AgCl (1.0 M KCl) reference electrode, respectively. This illustrates that the ultrathin defective hydrogenated TiO_2 shell in PtRu/TiO_2/ONCNT-400 indeed improves CO oxidation to surpass the state-of-the-art commercial PtRu/C catalysts, possibly by providing more −OH species near the Pt sites. The critical role of TiO_2 in PtRu/TiO_2/ONCNT-400 can be clearly observed by the earlier CO oxidation onset potential (by 35 mV lower) relative to PtRu/ONCNT-400 (without TiO_2). In addition, the SMSI illustrated by XPS, between PtRu and defective hydrogenated TiO_2/ONCNT support also contributes to enhancing the OH^- adsorption over the CO adsorption and thus lowers the CO oxidation potentials.

The ECSA of the catalysts was derived from the charge associated with the CO oxidation peak and mass of Pt on the electrode surface. Figure 4f presents the derived ECSA values of the four catalysts, which are 67.0 m^2/g_{Pt} for PtRu/TiO_2/ONCNT-400, 37.6 m^2/g_{Pt} for PtRu/ONCNT-400, 129.6 m^2/g_{Pt} for PtRu/C JM, and 99.5 m^2/g_{Pt} for PtRu/C TKK. The high ECSA of PtRu/C JM included an additional peak area associated with the oxidation of Pt or Ru catalysts in the subsequent CV (2^{nd}) cycle as shown in Figure 4a. Subtracting this contribution gives a corrected ECSA of 91.7 m^2/g_{Pt} for PtRu/C JM. The ECSA of PtRu/TiO_2/ONCNT-400 is higher than the PtRu/ONCNT-400, depicting better PtRu NP

https://doi.org/10.1021/acsanm.1c03742
ACS Appl. Nano Mater. 2022, 5, 3275−3288

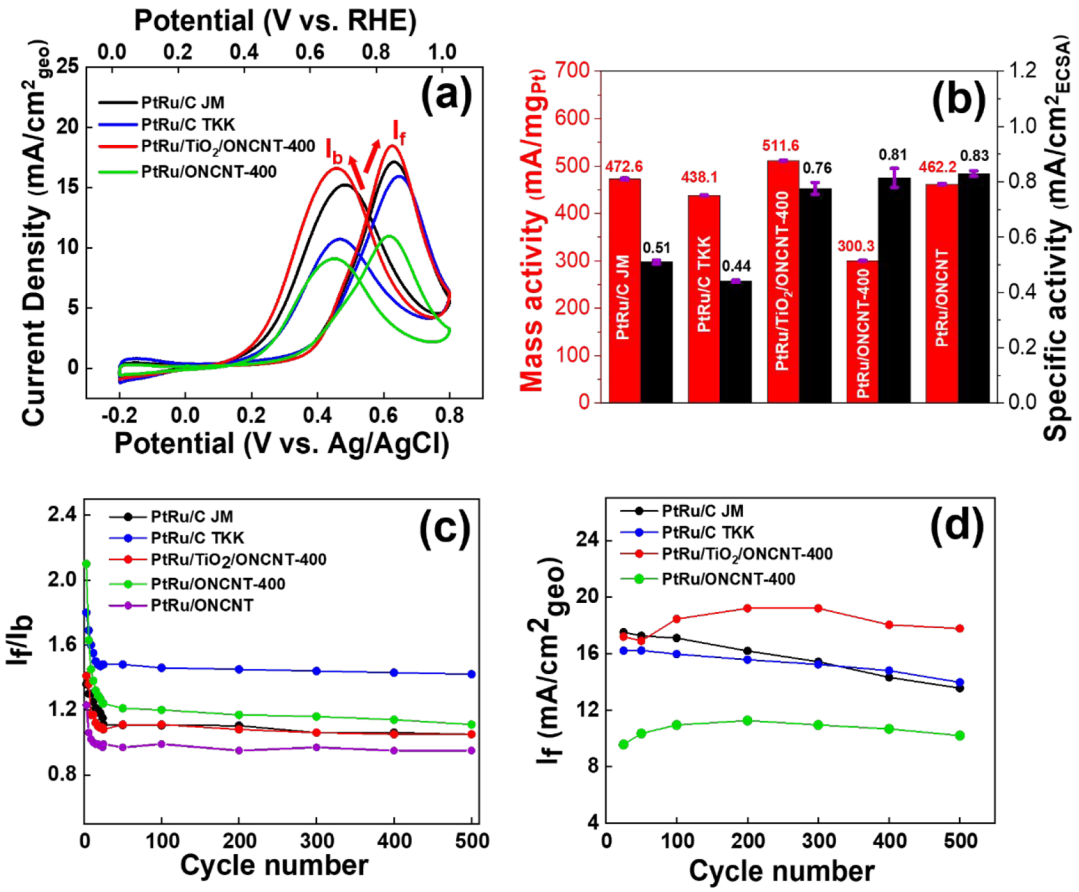

Figure 5. (a) Cyclic voltammetry curves (in the 100th cycle) of PtRu/ONCNT-400 and PtRu/TiO_2/ONCNT-400 in comparison with the two commercial PtRu/C catalyst from TKK and JM, with all PGM loading at 54 $\mu g/cm^2$, recorded in Ar-purged 0.50 M H_2SO_4 solution containing 0.75 M methanol at a scan rate of 50 mV/s. (b) The bar plot showing the mass activity and ECSA-normalized specific activity derived from CVs of the four catalysts in panel (a) and PtRu/ONCNT. (c) Plot of I_f/I_b ratio and (d) plot of I_f of the four catalysts in panel (a) versus the cycle number recorded in Ar-purged 0.50 M H_2SO_4 solution containing 0.75 M methanol at a scan rate of 50 mV/s. The filling solution in Ag/AgCl reference electrode is 1.0 M KCl.

dispersion on the TiO_2 shell. However, it is still lower than the commercial catalysts. As shown in Figure S14a, the CO oxidation peak potential of PtRu/TiO_2/ONCNT-400 (annealed at 400 °C) shifts by over −200 mV comparing to PtRu/TiO_2/ONCNT (unannealed). This reiterates the necessity of thermal annealing to improve the catalytic activity by forming PtRu alloy NPs and generating SMSI between PtRu and TiO_2. However, the ECSA of the PtRu/TiO_2/ONCNT-400 (67.0 m^2/g_{Pt}) is lower than the PtRu/TiO_2/ONCNT (unannealed), 75.0 m^2/g_{Pt}, due to the slight increase in the particle size during alloy formation by thermal annealing in 3% H_2/97% Ar atmosphere. The effects of nitrogen doping and oxygen functionalization in enhancing the CO oxidation kinetics are shown in Figure S14b. The earlier CO oxidation onset potential for PtRu/ONCNT when compared to PtRu/NCNT and PtRu/OCNT illustrates the synergistic of nitrogen doping and oxygen functionalization in improving the CO oxidation kinetics. The ECSA values of PtRu/ONCNT (55.5 m^2/g_{Pt}) are found to be higher than PtRu/OCNT (46.5 m^2/g_{Pt}) showing the better PtRu nanoparticle dispersion on NCNT support due to nitrogen anchoring sites. The critical role of Ru is further illustrated in Figure S15. For the catalysts without Ru, the CO stripping properties of Pt/TiO_2/ONCNT-400 are very similar to the commercial Pt/C JM catalyst, with the peak potential of 0.522 V vs 0.528 V (relative to Ag/AgCl (1.0 M KCl)), both are more than 300 mV higher than their PtRu counterparts. The ECSA values of these two Pt catalysts (58.7 m^2/g_{Pt} vs 56.6 m^2/g_{Pt}) are also very similar. This clearly illustrates the critical role of Ru in providing OH species at much lower potential which significantly enhances the CO oxidation kinetics of PtRu/TiO_2/ONCNT-400.

3.6. Assessment of the Catalytic Activity of MOR. The electrocatalytic performance in MOR was investigated by CV in Ar-saturated 0.50 M H_2SO_4 containing 0.75 M methanol solution at a PGM catalyst loading of 54 $\mu g/cm^2$. As shown in Figure 5a, a typical CV curve of MOR consists of two irreversible oxidation peaks, one in the forward anodic scan and the other in the backward cathodic scan. The forward peak current density (I_f) is attributed to the methanol oxidation on the Pt surface whereas the backward peak current density (I_b) is commonly attributed to the oxidation of carbonaceous intermediate species formed in the previous anodic scan.[65] However, some recent literature attributes the I_b to the methanol oxidation on regenerated Pt surface by reducing PtO_x formed in the high potential region (>0.6 V vs Ag/AgCl (1.0 M KCl) or 0.8 V vs RHE) of the previous forward scan, based on the fact that the I_b peak potential is strongly dependent on the upper potential limit in the CV.[19,66−68] Hence, the I_f/I_b ratio is associated with the degree of oxophilicity of the catalyst.[19]

https://doi.org/10.1021/acsanm.1c03742
ACS Appl. Nano Mater. 2022, 5, 3275−3288

Since the NCNTs were oxygenated before TiO_2 deposition, their effect on catalyst oxophilicity was first studied by comparing the MOR curves of Pt deposited on oxygenated and pristine NCNT support, i.e., Pt/ONCNT and Pt/NCNT, relative to the commercial Pt/C JM catalyst. To make it consistent, all CVs are from the 100th cycle after the catalyst is stabilized. As shown in Figure S16a, Pt/ONCNT has a higher I_f (9.17 mA/cm$^2_{geo}$) than Pt/NCNT (6.39 mA/cm$^2_{geo}$) but a similar I_f/I_b ratio of 1.1), both of which are higher than those of commercial Pt/C JM catalyst (I_f = 6.19 mA/cm$^2_{geo}$ and I_f/I_b = 0.6). This suggests that the additional oxygen functional groups in ONCNT and the intrinsic N-doping in pristine NCNT supports are effective in facilitating facile oxidation of carbonaceous species on the Pt surface and thereby improving the MOR kinetics.[11,19,20] Similarly, the MOR curves of PtRu/NCNT and PtRu/ONCNT are compared to study the contribution of Ru and ONCNTs in MOR, as shown in Figure S16b. The I_f values are 17.20 mA/cm$^2_{geo}$ for PtRu/C JM, 16.64 mA/cm$^2_{geo}$ for PtRu/ONCNT, and 12.58 mA/cm$^2_{geo}$ for PtRu/NCNT, which are substantially higher than the counterparts without Ru, while the I_f/I_b ratios maintain at about 1.1, 1.1, and 1.0. These results agree well with the recent reports that the oxygen functional groups in the carbon support improves the oxophilicity of the catalyst.[19,20]

The catalytic MOR after TiO_2 deposition on ONCNT was then studied following the same protocol. Figure 5a presents the MOR curves from the 100th CV cycle for the PtRu/TiO_2/ONCNT-400 and PtRu/ONCNT-400 in comparison with the commercial PtRu/C catalysts from JM and TKK. The PtRu/TiO_2/ONCNT-400 catalyst exhibits the highest I_f (18.61 mA/cm$^2_{geo}$) that outperforms not only PtRu/ONCNT-400 (10.90 mA/cm$^2_{geo}$) but also commercial PtRu/C JM (17.20 mA/cm$^2_{geo}$) and PtRu/C TKK (15.91 mA/cm$^2_{geo}$). These trends corroborate with the corresponding CO stripping voltammetry. It is noteworthy that thermal annealing of PtRu/ONCNT causes significant drop in the I_f value from 16.64 mA/cm$^2_{geo}$ in Figure S16b to 10.90 mA/cm$^2_{geo}$ for PtRu/ONCNT-400 in Figure 5a, mainly due to PGM agglomeration without the hydrogenated TiO_2 shell as we discussed above.

It is to be noted that the I_f/I_b ratio is much higher in the first few CV cycles but decreases fast within the initial 25 CV cycles (as shown in Figure 5c). Most studies in literature only report the CVs in the early cycles. For comparison with literature, the MOR curves recorded at the third CV cycle of the above catalysts are shown in Figure S17. The I_f/I_b ratio is found to be 1.4 for PtRu/TiO_2/ONCNT-400, 2.1 for PtRu/ONCNT-400, 1.4 for PtRu/C JM, and 1.8 for PtRu/C TKK, respectively. The PtRu/TiO_2/ONCNT-400 shows an I_f/I_b of 1.4 in the initial cycles and maintains I_f/I_b > 1 until 500 cycles (shown in Figure 5c). Typically in literature, only PtRu/C catalysts having high oxophilicity show an I_f/I_b > 1, is attributed to the tendency to form more oxygenated species that enhance oxidization of the poisonous CO intermediate.[67] The MOR activity of PtRu/TiO_2/ONCNT (unannealed) catalyst is compared with PtRu/TiO_2/ONCNT-400 in Figure S18a. The I_f of PtRu/TiO_2/ONCNT-400 (18.61 mA/cm$^2_{geo}$) is slightly higher than that of the unannealed PtRu/TiO_2/ONCNT (18.54 mA/cm$^2_{geo}$), but the I_f/I_b of PtRu/TiO_2/ONCNT-400 (1.1) is significantly higher than that of PtRu/TiO_2/ONCNT (0.9). Thermal annealing the catalyst in 3% H_2/97% Ar is critical in enhancing the oxophilicity of the catalyst, likely by the combined effects of forming defective hydrogenated ultrathin TiO_2 shell and crystalline PtRu alloy. Interestingly, if Ru is not included, the Pt catalyst Pt/TiO_2/ONCNT-400 produces a substantially higher I_f (8.73 mA/cm$^2_{geo}$) than the commercial Pt/C JM catalyst (6.20 mA/cm$^2_{geo}$), as shown in Figure S18b. Clearly, the TiO_2 shell provides certain degree of oxophilicity that helps to mitigate CO poisoning on Pt catalysts. Figure S18c shows that MOR CV curve of TiO_2/ONCNT without Pt or PtRu deposition. TiO_2/ONCNT alone does not show measurable catalytic activity toward MOR. It only serves as a hybrid support to enhance the catalytic activity of PtRu NPs.

Additional insights into the catalysts are illustrated in Figure 5b, which summarizes the mass activity, defined by the measured geometric current density I_f (mA/cm^2) divided by the mass loading of Pt (mg$_{pt}$/cm^2), and the ECSA-normalized specific activity, defined by I_f (mA/cm^2) divided by the product of ECSA (m^2/g$_{Pt}$) and Pt loading (mg$_{pt}$/cm^2) on the electrode surface. PtRu/TiO_2/ONCNT-400 showed the highest mass activity of 511.6 mA/mg$_{Pt}$, which surpasses the two state-of-the-art commercial PtRu/C catalysts from JM (472.6 mA/mg$_{Pt}$), TKK (438.1 mA/mg$_{Pt}$) and PtRu/ONCNTs-400 (300.3 mA/mg$_{Pt}$). In terms of ECSA-normalized specific activity, PtRu/TiO_2/ONCNT-400 exceeds the commercial PtRu/C catalysts even more, giving a value of 0.76 mA/cm$^2_{ECSA}$, which is about 1.5-fold of the commercial PtRu/C JM catalyst (0.51 mA/cm$^2_{ECSA}$) and 1.7-fold of PtRu/C TKK catalyst (0.44 mA/cm$^2_{ECSA}$). This is largely due to its ability to present a slightly higher mass activity at the much lower ECSA. The PtRu/ONCNT-400 catalyst (without the TiO_2 coating) shows an even higher ECSA-normalized specific activity but suffers from a low mass activity due to its very low ECSA. Balancing all the trading factors, PtRu/TiO_2/ONCNT-400 shows the highest MOR catalytic activity. Its mass activity can be further enhanced by increasing its ECSA in the future.

The long-term stability is another important characteristic to evaluate the MOR catalysts for DMFC applications. In this study, the long-term stability of the in-house prepared PtRu/TiO_2/ONCNT-400, PtRu/ONCNT and PtRu/ONCNT-400 catalysts were evaluated and compared with the two commercial PtRu/C catalysts from JM and TKK by monitoring the I_f/I_b ratio and I_f values over 500 consecutive CV cycles, as shown in Figure 5c,d. In Figure 5c, all five catalysts show rapid decrease in I_f/I_b ratio in the initial 25 cycles but become stabilized after the 25th cycle, being able to retain 97.3%, 96.0%, 89.5%, 94.6%, and 95.9% until the 500th cycle, indicating that the degree of oxophilicity of the catalysts did not have significant change from the 25th cycle to 500th cycle. PtRu/TiO_2/ONCNT-400 and PtRu/ONCNT-400 have the similar I_f/I_b values as PtRu/C JM while that of PtRu/C TKK is somehow much higher though it did not lead to higher MOR mass activity in Figure 5b. In Figure 5d, the I_f value of the two commercial PtRu/C catalysts steadily decreases over time during the 500 cycles, giving a 20.7% drop for PtRu/C JM and 12.5% drop for PtRu/C TKK. In contrast, the two in-house prepared catalysts PtRu/TiO_2/ONCNT-400 and PtRu/ONCNT-400 show drastically different behaviors. Their I_f values increase in the first 100 to 200 cycles (due to catalyst activation) and then become relatively stable over the rest cycles, giving only 3.6% and 6.8% drop from the highest point in the 500th cycle. More importantly, the I_f value of PtRu/TiO_2/ONCNT-400 is about 20% higher than the two state-of-the-art PtRu/C catalysts from the 200th to 500th cycles. In addition, the MOR stability of the PtRu/TiO_2/ONCNT-400, commercial PtRu/C JM, and PtRu/C TKK catalyst was also

https://doi.org/10.1021/acsanm.1c03742
ACS Appl. Nano Mater. 2022, 5, 3275−3288

evaluated by chronoamperometric measurements at a constant potential of 0.62 V vs Ag/AgCl (1.0 M KCl), as shown in Figure S19a. The rapid loss in the initial MOR current was observed for all catalysts, which is due to the formation and poisoning of catalyst surface by the intermediate carbonaceous species. The PtRu/TiO_2/ONCNT-400 showed a slower loss in initial current when compared to commercial PtRu/C JM and PtRu/C TKK.

Electrochemical impedance spectroscopy (EIS) measurements (see more details in ESI) of PtRu/TiO_2/ONCNT-400, PtRu/ONCNT-400, commercial PtRu/C JM, and PtRu/C TKK are shown in Figures S19b,c. The corresponding equivalent circuit for fitting the EIS is shown in Figure S19d and fitted values are shown in Table S5. The main electronic charge transfer resistance (R_1) for PtRu/TiO_2/ONCNT-400 was found to be 4.45 Ω, which is lower than the PtRu/ONCNT-400 without TiO_2 (32.5 Ω), commercial PtRu/C JM (21.8 Ω) and PtRu/C TKK (18.3 Ω). This reveals that PtRu NPS in PtRu/TiO_2/ONCNT-400 have superior charge transfer kinetics owing to its SMSI and increased charge density provided by the hydrogenated TiO_2 shell (as evidenced in XPS). The small increase in the serial resistance (R_s) may be due to the inclusion of ultrathin TiO_2 shell on ONCNT. But the value is very small and its effect is negligible.

These studies display that PtRu/TiO_2/ONCNT-400 shows an excellent stability and a higher electrocatalytic activity toward MOR which can be attributed to the strong attachment of PtRu on the ultrathin defective hydrogenated TiO_2 shell on ONCNT support and the SMSI due to chemical interaction and electron transfer from hydrogenated TiO_2 to the PGM NPs.

4. CONCLUSIONS

We have demonstrated the synthesis of a multifunctional hybrid catalyst support for PtRu-based MOR catalysts. A thin disordered hydrogenated TiO_2 shell is deposited on the oxygenated N-doped carbon nanotube by rapid microwave-assisted synthesis based on specific heating of the carbon core. PtRu nanoparticles are further deposited on the exterior surface of the hydrogenated TiO_2 shell by another microwave-assisted synthesis step. The hydrogenated TiO_2 shell is found to exhibit a strong interaction with the PtRu nanoparticles and is effective in retaining them in place and avoiding agglomeration during the thermal annealing at 400 °C. The optimal catalyst consists of crystalline PtRu alloy nanoparticles of ~3.8 nm in diameter anchored on the amorphous defective hydrogenated TiO_2 shell, denoted as PtRu/TiO_2/ONCNT-400. XPS spectra reveal that there is a partial electron transfer from defective hydrogenated TiO_2 support to PtRu catalyst which is consistent with the observed lower CO stripping onset potential. The synergistic effects of electron transfer and the increased oxophilicity provided by the defective hydrogenated TiO_2 support help to accelerate the CO oxidation and lead to higher mass activity and higher ECSA-specific activity in methanol oxidation than the two state-of-the-art commercial PtRu/C catalysts from JM and TKK. Furthermore, the PtRu/TiO_2/ONCNT-400 catalyst is much more stable than the commercial catalysts in the long cycles. It is a very promising anode catalyst for future DMFCs.

■ ASSOCIATED CONTENT

Supporting Information

The Supporting Information is available free of charge at https://pubs.acs.org/doi/10.1021/acsanm.1c03742.

TEM images of NCNT, ONCNT, TiO_2/ONCNT-400, commercial (PtRu/C JM and TKK) catalysts; HAADF-STEM elemental mapping of TiO_2/ONCNT; TEM images and particle size distribution of PtRu/TiO_2/ONCNT-400, Pt/ONCNT, Pt/TiO_2/ONCNT, Pt/TiO_2/ONCNT-400, PtRu/ONCNT, PtRu/TiO_2/ONCNT, Pt/ONCNT-400, and PtRu/ONCNT-400; TGA curves and calculations of commercial (PtRu/C JM and TKK) catalysts, PtRu/TiO_2/ONCNT-400, and its control samples; XRD patterns of commercial catalysts and control samples compared with PtRu/TiO_2/ONCNT-400; XPS characterization of NCNT, ONCNT, TiO_2/ONCNT, TiO_2/ONCNT-400, commercial catalysts, and PtRu/TiO_2/ONCNT-400; CO stripping voltammetry curves of PtRu/TiO_2/ONCNT, PtRu/TiO_2/ONCNT-400, Pt/TiO_2/ONCNT-400, and Pt/C JM. MOR CV curves of Pt and PtRu deposited on NCNT, ONCNT, TiO_2/ONCNT-400, commercial Pt/C JM, PtRu/C JM, and PtRu/C TKK; chronoamperometry and electrochemical impedance spectroscopy measurements of PtRu/TiO_2/ONCNT-400, PtRu/ONCNT-400, and commercial PtRu/C JM and TKK; table with EIS fitting parameters values; and table comparing the MOR electrochemical activity of PtRu/TiO_2/ONCNT-400 with various literatures (PDF)

■ AUTHOR INFORMATION

Corresponding Author

Jun Li − *Department of Chemistry, Kansas State University, Manhattan, Kansas 66506, United States;* orcid.org/0000-0002-3689-8946; Email: junli@ksu.edu

Authors

Archana Sekar − *Department of Chemistry, Kansas State University, Manhattan, Kansas 66506, United States;* orcid.org/0000-0003-2171-7900

Nathaniel Metzger − *Department of Mechanical Engineering, University of Kansas School of Engineering, Lawrence, Kansas 66045, United States*

Sabari Rajendran − *Department of Chemistry, Kansas State University, Manhattan, Kansas 66506, United States*

Ayyappan Elangovan − *Department of Chemistry, Kansas State University, Manhattan, Kansas 66506, United States;* orcid.org/0000-0002-0985-2475

Yonghai Cao − *School of Chemistry and Chemical Engineering, Guangdong Provincial Key Lab of Green Chemical Product Technology, South China University of Technology, Guangzhou 510640, P. R. China;* orcid.org/0000-0003-0035-6253

Feng Peng − *School of Chemistry and Chemical Engineering, Guangzhou University, Guangzhou 510006, P. R. China;* orcid.org/0000-0002-5154-6666

Xianglin Li − *Department of Mechanical Engineering, University of Kansas School of Engineering, Lawrence, Kansas 66045, United States;* orcid.org/0000-0002-0193-9410

Complete contact information is available at: https://pubs.acs.org/10.1021/acsanm.1c03742

https://doi.org/10.1021/acsanm.1c03742
ACS Appl. Nano Mater. 2022, 5, 3275−3288

Author Contributions

A.S.: methodology, investigation, formal analysis, validation, and writing−original draft. N.M.: resources and investigation. S.R.: visualization and writing−review and editing. A.E.: writing−review and editing. Y.C.: resources, methodology, and writing−review and editing. F.P.: resources, methodology, and writing−review and editing. X.L.: resources, investigation, writing−review and editing and funding acquisition. J.L.: conceptualization, methodology, validation, supervision, writing−review and editing, and funding acquisition.

Funding

This work was supported by the US Department of Energy (DOE) grant DE-EE0008440 and in part by the US National Science Foundation grant CBET-1703263.

Notes

The authors declare no competing financial interest.

■ ACKNOWLEDGMENTS

This work was supported by the US Department of Energy (DOE) grant DE-EE0008440 and in part by the US National Science Foundation grant CBET-1703263. We would like to thank Dr. Balasubramanian Balamurugan from the University of Nebraska and Dr. Prem Thapa from the University of Kansas, for the XPS measurements. We would also like to thank Prof. Christer Aakeroy and Kelly Shunje at Kansas State University for support in TGA measurements. The XPS and HRTEM characterization were performed in part in the Nebraska Nanoscale Facility: National Nanotechnology Coordinated Infrastructure and the Nebraska Center for Materials and Nanoscience (and/or NERCF), which are supported by the US National Science Foundation under Award ECCS: 2025298, and the Nebraska Research Initiative.

■ REFERENCES

(1) Feng, Y.; Liu, H.; Yang, J. A selective electrocatalyst−based direct methanol fuel cell operated at high concentrations of methanol. *Sci. Adv.* **2017**, *3* (6), e1700580.

(2) Stamenkovic, V. R.; Strmcnik, D.; Lopes, P. P.; Markovic, N. M. Energy and fuels from electrochemical interfaces. *Nat. Mater.* **2017**, *16* (1), 57−69.

(3) Garg, A.; Milina, M.; Ball, M.; Zanchet, D.; Hunt, S. T.; Dumesic, J. A.; Román-Leshkov, Y. Transition-Metal Nitride Core@Noble-Metal Shell Nanoparticles as Highly CO Tolerant Catalysts. *Angew. Chem., Int. Ed.* **2017**, *56* (30), 8828−8833.

(4) Cui, X.; Zhu, Y.; Hua, Z.; Feng, J.; Liu, Z.; Chen, L.; Shi, J. SnO2 nanocrystal-decorated mesoporous ZSM-5 as a precious metal-free electrode catalyst for methanol oxidation. *Energy Environ. Sci.* **2015**, *8* (4), 1261−1266.

(5) Ouyang, Y.; Cao, H.; Wu, H.; Wu, D.; Wang, F.; Fan, X.; Yuan, W.; He, M.; Zhang, L. Y.; Li, C. M. Tuning Pt-skinned PtAg nanotubes in nanoscales to efficiently modify electronic structure for boosting performance of methanol electrooxidation. *Applied Catalysis B: Environmental* **2020**, *265*, 118606.

(6) Chen, D.-J.; Tong, Y. J. Irrelevance of Carbon Monoxide Poisoning in the Methanol Oxidation Reaction on a PtRu Electrocatalyst. *Angew. Chem., Int. Ed.* **2015**, *54* (32), 9394−9398.

(7) Kaur, A.; Kaur, G.; Singh, P. P.; Kaushal, S. Supported bimetallic nanoparticles as anode catalysts for direct methanol fuel cells: A review. *Int. J. Hydrogen Energy* **2021**, *46* (29), 15820−15849.

(8) Wang, Q.; Chen, S.; Li, P.; Ibraheem, S.; Li, J.; Deng, J.; Wei, Z. Surface Ru enriched structurally ordered intermetallic PtFe@PtRuFe core-shell nanostructure boosts methanol oxidation reaction catalysis. *Applied Catalysis B: Environmental* **2019**, *252*, 120−127.

(9) Yu, P. T.; Gu, W.; Makharia, R.; Wagner, F. T.; Gasteiger, H. A. The Impact of Carbon Stability on PEM Fuel Cell Startup and Shutdown Voltage Degradation. *ECS Trans.* **2006**, *3* (1), 797−809.

(10) Zhang, Z.; Liu, J.; Gu, J.; Su, L.; Cheng, L. An overview of metal oxide materials as electrocatalysts and supports for polymer electrolyte fuel cells. *Energy Environ. Sci.* **2014**, *7* (8), 2535−2558.

(11) Ning, X.; Li, Y.; Dong, B.; Wang, H.; Yu, H.; Peng, F.; Yang, Y. Electron transfer dependent catalysis of Pt on N-doped carbon nanotubes: Effects of synthesis method on metal-support interaction. *J. Catal.* **2017**, *348*, 100−109.

(12) Chen, Y.; Wang, J.; Liu, H.; Banis, M. N.; Li, R.; Sun, X.; Sham, T.-K.; Ye, S.; Knights, S. Nitrogen Doping Effects on Carbon Nanotubes and the Origin of the Enhanced Electrocatalytic Activity of Supported Pt for Proton-Exchange Membrane Fuel Cells. *J. Phys. Chem. C* **2011**, *115* (9), 3769−3776.

(13) Saha, M. S.; Li, R.; Sun, X.; Ye, S. 3-D composite electrodes for high performance PEM fuel cells composed of Pt supported on nitrogen-doped carbon nanotubes grown on carbon paper. *Electrochem. Commun.* **2009**, *11* (2), 438−441.

(14) Li, S.; Shu, J.; Ma, S.; Yang, H.; Jin, J.; Zhang, X.; Jin, R. Engineering three-dimensional nitrogen-doped carbon black embedding nitrogen-doped graphene anchoring ultrafine surface-clean Pd nanoparticles as efficient ethanol oxidation electrocatalyst. *Applied Catalysis B: Environmental* **2021**, *280*, 119464.

(15) Yang, H.; Zhang, X.; Zou, H.; Yu, Z.; Li, S.; Sun, J.; Chen, S.; Jin, J.; Ma, J. Palladium Nanoparticles Anchored on Three-Dimensional Nitrogen-Doped Carbon Nanotubes as a Robust Electrocatalyst for Ethanol Oxidation. *ACS Sustainable Chem. Eng.* **2018**, *6* (6), 7918−7923.

(16) Chetty, R.; Kundu, S.; Xia, W.; Bron, M.; Schuhmann, W.; Chirila, V.; Brandl, W.; Reinecke, T.; Muhler, M. PtRu nanoparticles supported on nitrogen-doped multiwalled carbon nanotubes as catalyst for methanol electrooxidation. *Electrochim. Acta* **2009**, *54* (17), 4208−4215.

(17) Zhang, J.; Lu, S.; Xiang, Y.; Jiang, S. P. Intrinsic Effect of Carbon Supports on the Activity and Stability of Precious Metal Based Catalysts for Electrocatalytic Alcohol Oxidation in Fuel Cells: A Review. *ChemSusChem* **2020**, *13* (10), 2484−2502.

(18) Liu, D.; Yang, G.; Zhang, Q.; Wang, H.; Yu, H.; Peng, F. Highly Enhanced Methanol Electrooxidation on Pt/N−CNT-Decorated FeP**. *ChemElectroChem.* **2021**, *8* (13), 2442−2448.

(19) Elangovan, A.; Xu, J.; Sekar, A.; Liu, B.; Li, J. Enhancing Methanol Oxidation Reaction with Platinum-based Catalysts using a N-Doped Three-dimensional Graphitic Carbon Support. *ChemCatChem.* **2020**, *12* (23), 6000−6012.

(20) Xiong, W.; Mehrabadi, B. A. T.; Karakolos, S. G.; White, R. D.; Shakouri, A.; Kasak, P.; Zaidi, S. J.; Weidner, J. W.; Regalbuto, J. R.; Colon-Mercado, H.; Monnier, J. R. Enhanced Performance of Oxygen-Functionalized Multiwalled Carbon Nanotubes as Support for Pt and Pt−Ru Bimetallic Catalysts for Methanol Electrooxidation. *ACS Applied Energy Materials* **2020**, *3* (6), 5487−5496.

(21) Ioroi, T.; Senoh, H.; Yamazaki, S.-i.; Siroma, Z.; Fujiwara, N.; Yasuda, K. Stability of Corrosion-Resistant Magnéli-Phase Ti[sub 4]O[sub 7]-Supported PEMFC Catalysts at High Potentials. *J. Electrochem. Soc.* **2008**, *155* (4), B321.

(22) Jiang, Z.-Z.; Wang, Z.-B.; Chu, Y.-Y.; Gu, D.-M.; Yin, G.-P. Ultrahigh stable carbon riveted Pt/TiO2−C catalyst prepared by in situ carbonized glucose for proton exchange membrane fuel cell. *Energy Environ. Sci.* **2011**, *4* (3), 728−735.

(23) Wang, W.; Wang, H.; Key, J.; Linkov, V.; Ji, S.; Wang, R. Nanoparticulate TiO2-promoted PtRu/C catalyst for methanol oxidation. *Ionics* **2013**, *19* (3), 529−534.

(24) Wang, Z.; Chen, G.; Xia, D.; Zhang, L. Studies on the electrocatalytic properties of PtRu/C-TiO2 toward the oxidation of methanol. *J. Alloys Compd.* **2008**, *450* (1), 148−151.

(25) Shanmugam, S.; Gedanken, A. Carbon-Coated Anatase TiO2 Nanocomposite as a High-Performance Electrocatalyst Support. *Small* **2007**, *3* (7), 1189−1193.

https://doi.org/10.1021/acsanm.1c03742
ACS Appl. Nano Mater. 2022, 5, 3275−3288

(26) Huang, S.-Y.; Ganesan, P.; Park, S.; Popov, B. N. Development of a Titanium Dioxide-Supported Platinum Catalyst with Ultrahigh Stability for Polymer Electrolyte Membrane Fuel Cell Applications. *J. Am. Chem. Soc.* **2009**, *131* (39), 13898−13899.
(27) Myung, S.-T.; Kikuchi, M.; Yoon, C. S.; Yashiro, H.; Kim, S.-J.; Sun, Y.-K.; Scrosati, B. Black anatase titania enabling ultra high cycling rates for rechargeable lithium batteries. *Energy Environ. Sci.* **2013**, *6* (9), 2609−2614.
(28) Ioroi, T.; Siroma, Z.; Fujiwara, N.; Yamazaki, S.-i.; Yasuda, K. Sub-stoichiometric titanium oxide-supported platinum electrocatalyst for polymer electrolyte fuel cells. *Electrochem. Commun.* **2005**, *7* (2), 183−188.
(29) Bartholomew, R. F.; Frankl, D. R. Electrical Properties of Some Titanium Oxides. *Phys. Rev.* **1969**, *187* (3), 828−833.
(30) Huang, S.-Y.; Ganesan, P.; Popov, B. N. Electrocatalytic activity and stability of niobium-doped titanium oxide supported platinum catalyst for polymer electrolyte membrane fuel cells. *Applied Catalysis B: Environmental* **2010**, *96* (1), 224−231.
(31) Qin, Y.-H.; Li, Y.; Lv, R.-L.; Wang, T.-L.; Wang, W.-G.; Wang, C.-W. Enhanced methanol oxidation activity and stability of Pt particles anchored on carbon-doped TiO2 nanocoating support. *J. Power Sources* **2015**, *278*, 639−644.
(32) Kim, J. H.; Cho, E.; Jang, J. H.; Kim, H.; Lim, T.; Oh, I.; Ko, J. J.; Oh, S. C. *J. Electrochem. Soc.* **2010**, *157*, B104.
(33) Huang, K.; Sasaki, K.; Adzic, R. R.; Xing, Y. Increasing Pt oxygen reduction reaction activity and durability with a carbon-doped TiO2 nanocoating catalyst support. *J. Mater. Chem.* **2012**, *22* (33), 16824−16832.
(34) Chen, X.; Liu, L.; Yu, P. Y.; Mao, S. S. Increasing Solar Absorption for Photocatalysis with Black Hydrogenated Titanium Dioxide Nanocrystals. *Science* **2011**, *331* (6018), 746.
(35) Gao, J.; Xue, J.; Jia, S.; Shen, Q.; Zhang, X.; Jia, H.; Liu, X.; Li, Q.; Wu, Y. Self-Doping Surface Oxygen Vacancy-Induced Lattice Strains for Enhancing Visible Light-Driven Photocatalytic H2 Evolution over Black TiO2. *ACS Appl. Mater. Interfaces* **2021**, *13* (16), 18758−18771.
(36) Haerudin, H.; Bertel, S.; Kramer, R. Surface stoichiometry of 'titanium suboxide' Part I Volumetric and FTIR study. *Journal of the Chemical Society, Faraday Transactions* **1998**, *94* (10), 1481−1487.
(37) Eder, D.; Kramer, R. Stoichiometry of "titanium suboxide" Part 2. Electric properties. *Phys. Chem. Chem. Phys.* **2003**, *5* (6), 1314−1319.
(38) Zhang, C.; Yu, H.; Li, Y.; Gao, Y.; Zhao, Y.; Song, W.; Shao, Z.; Yi, B. Supported Noble Metals on Hydrogen-Treated TiO2 Nanotube Arrays as Highly Ordered Electrodes for Fuel Cells. *ChemSusChem* **2013**, *6* (4), 659−666.
(39) Nunez, P.; Richter, M. H.; Piercy, B. D.; Roske, C. W.; Cabán-Acevedo, M.; Losego, M. D.; Konezny, S. J.; Fermin, D. J.; Hu, S.; Brunschwig, B. S.; Lewis, N. S. Characterization of Electronic Transport through Amorphous TiO2 Produced by Atomic Layer Deposition. *J. Phys. Chem. C* **2019**, *123* (33), 20116−20129.
(40) Chimupala, Y.; Hyett, G.; Simpson, R.; Mitchell, R.; Douthwaite, R.; Milne, S. J.; Brydson, R. D. Synthesis and characterization of mixed phase anatase TiO2 and sodium-doped TiO2(B) thin films by low pressure chemical vapour deposition (LPCVD). *RSC Adv.* **2014**, *4* (89), 48507−48515.
(41) Kitano, M.; Mitsui, R.; Eddy, D. R.; El-Bahy, Z. M. A.; Matsuoka, M.; Ueshima, M.; Anpo, M. Synthesis of Nanowire TiO2 Thin Films by Hydrothermal Treatment and their Photoelectrochemical Properties. *Catal. Lett.* **2007**, *119* (3), 217−221.
(42) Lee, S.-H.; Kang, M.; Cho, S. M.; Han, G. Y.; Kim, B.-W.; Yoon, K. J.; Chung, C.-H. Synthesis of TiO2 photocatalyst thin film by solvothermal method with a small amount of water and its photocatalytic performance. *J. Photochem. Photobiol., A* **2001**, *146* (1), 121−128.
(43) Tsuji, M. Microwave-Assisted Synthesis of Metallic Nanomaterials in Liquid Phase. *ChemistrySelect* **2017**, *2* (2), 805−819.
(44) Reeja-Jayan, B.; Harrison, K. L.; Yang, K.; Wang, C.-L.; Yilmaz, A. E.; Manthiram, A. Microwave-assisted Low-temperature Growth of Thin Films in Solution. *Sci. Rep.* **2012**, *2* (1), 1003.
(45) Vigil, E.; Saadoun, L.; Ayllón, J. A.; Domènech, X.; Zumeta, I.; Rodríguez-Clemente, R. TiO2 thin film deposition from solution using microwave heating. *Thin Solid Films* **2000**, *365* (1), 12−18.
(46) Kang, S.; Fan Xia; Zhuofeng Hu; Hu, W.; She, Y.; Wang, L.; Fu, X.; Lu, W. Platinum nanoparticles with TiO2−skin as a durable catalyst for photoelectrochemical methanol oxidation and electrochemical oxygen reduction reactions. *Electrochim. Acta* **2020**, *343*, 136119.
(47) Zhu, H.; Chen, J.; Li, X.; Liu, Y.; Gao, L.; Chen, J. Homogenous decoration of Pt and PtSn alloy nanoparticles onto multi-walled carbon nanotubes. *Materials Research Express* **2019**, *6* (11), 115048.
(48) Garcia, G.; Baglio, V.; Stassi, A.; Pastor, E.; Antonucci, V.; Aricò, A. S. Investigation of Pt−Ru nanoparticle catalysts for low temperature methanol electro-oxidation. *J. Solid State Electrochem.* **2007**, *11* (9), 1229−1238.
(49) Antolini, E.; Cardellini, F. Formation of carbon supported PtRu alloys: an XRD analysis. *J. Alloys Compd.* **2001**, *315* (1), 118−122.
(50) Radmilovic, V.; Gasteiger, H. A.; Ross, P. N. Structure and Chemical Composition of a Supported Pt-Ru Electrocatalyst for Methanol Oxidation. *J. Catal.* **1995**, *154* (1), 98−106.
(51) Holzwarth, U.; Gibson, N. The Scherrer equation versus the 'Debye-Scherrer equation'. *Nat. Nanotechnol.* **2011**, *6* (9), 534−534.
(52) Zhang, L.; Wang, X.; Wang, R.; Hong, M. Structural Evolution from Metal−Organic Framework to Hybrids of Nitrogen-Doped Porous Carbon and Carbon Nanotubes for Enhanced Oxygen Reduction Activity. *Chem. Mater.* **2015**, *27* (22), 7610−7618.
(53) Zhao, M.; Cao, Y.; Liu, X.; Deng, J.; Li, D.; Gu, H. Effect of nitrogen atomic percentage on N+-bombarded MWCNTs in cytocompatibility and hemocompatibility. *Nanoscale Res. Lett.* **2014**, *9* (1), 142.
(54) Chen, C.; Zhang, J.; Zhang, B.; Yu, C.; Peng, F.; Su, D. Revealing the enhanced catalytic activity of nitrogen-doped carbon nanotubes for oxidative dehydrogenation of propane. *Chem. Commun.* **2013**, *49* (74), 8151−8153.
(55) Kundu, S.; Xia, W.; Busser, W.; Becker, M.; Schmidt, D. A.; Havenith, M.; Muhler, M. The formation of nitrogen-containing functional groups on carbon nanotube surfaces: a quantitative XPS and TPD study. *Phys. Chem. Chem. Phys.* **2010**, *12* (17), 4351−4359.
(56) Borbón-Nuñez, H. A.; Muñiz, J.; El Hachimi, A. G.; Frausto-Silva, D.; Gutiérrez-Díaz, J. L.; Domínguez, D.; Tiznado, H.; Cuentas-Gallegos, A. K. Effect of oxygen based functional groups on the nucleation of TiO2 by atomic layer deposition: A theoretical and experimental study. *Mater. Chem. Phys.* **2021**, *267*, 124588.
(57) Zhao, A.; Masa, J.; Xia, W. Very low amount of TiO2 on N-doped carbon nanotubes significantly improves oxygen reduction activity and stability of supported Pt nanoparticles. *Phys. Chem. Chem. Phys.* **2015**, *17* (16), 10767−10773.
(58) Zheng, Z.; Huang, B.; Lu, J.; Wang, Z.; Qin, X.; Zhang, X.; Dai, Y.; Whangbo, M.-H. Hydrogenated titania: synergy of surface modification and morphology improvement for enhanced photocatalytic activity. *Chem. Commun.* **2012**, *48* (46), 5733−5735.
(59) Nagatsuka, N.; Wilde, M.; Fukutani, K. Hydrogenation and hydrogen diffusion at the anatase TiO2(101) surface. *J. Chem. Phys.* **2020**, *152* (7), 074708.
(60) Wang, C.; Yang, J.; Li, T.; Shen, Z.; Guo, T.; Zhang, H.; Lu, Z. In Situ Tuning of Defects and Phase Transition in Titanium Dioxide by Lithiothermic Reduction. *ACS Appl. Mater. Interfaces* **2020**, *12* (5), 5750−5758.
(61) Pham, H. H.; Wang, L.-W. Oxygen vacancy and hole conduction in amorphous TiO2. *Phys. Chem. Chem. Phys.* **2015**, *17* (1), 541−550.
(62) Hu, S.; Shaner, M. R.; Beardslee, J. A.; Lichterman, M.; Brunschwig, B. S.; Lewis, N. S. Amorphous TiO_2 coatings stabilize Si, GaAs, and GaP photoanodes for efficient water oxidation. *Science* **2014**, *344* (6187), 1005.

https://doi.org/10.1021/acsanm.1c03742
ACS Appl. Nano Mater. 2022, 5, 3275−3288

(63) Matin, M. A.; Lee, E.; Kim, H.; Yoon, W.-S.; Kwon, Y.-U. Rational syntheses of core−shell Fe@(PtRu) nanoparticle electrocatalysts for the methanol oxidation reaction with complete suppression of CO-poisoning and highly enhanced activity. *Journal of Materials Chemistry A* **2015**, *3* (33), 17154−17164.
(64) Guo, J. W.; Zhao, T. S.; Prabhuram, J.; Chen, R.; Wong, C. W. Preparation and characterization of a PtRu/C nanocatalyst for direct methanol fuel cells. *Electrochim. Acta* **2005**, *51* (4), 754−763.
(65) Mancharan, R.; Goodenough, J. B. Methanol oxidation in acid on ordered NiTi. *J. Mater. Chem.* **1992**, *2* (8), 875−887.
(66) Hofstead-Duffy, A. M.; Chen, D.-J.; Sun, S.-G.; Tong, Y. J. Origin of the current peak of negative scan in the cyclic voltammetry of methanol electro-oxidation on Pt-based electrocatalysts: a revisit to the current ratio criterion. *J. Mater. Chem.* **2012**, *22* (11), 5205−5208.
(67) Chung, D. Y.; Lee, K.-J.; Sung, Y.-E. Methanol Electro-Oxidation on the Pt Surface: Revisiting the Cyclic Voltammetry Interpretation. *J. Phys. Chem. C* **2016**, *120* (17), 9028−9035.
(68) Lai, L.; Yang, G.; Zhang, Q.; Yu, H.; Peng, F. Essential analysis of cyclic voltammetry of methanol electrooxidation using the differential electrochemical mass spectrometry. *J. Power Sources* **2021**, *509*, 230397.

https://doi.org/10.1021/acsanm.1c03742
ACS Appl. Nano Mater. 2022, 5, 3275−3288